Physical investigations on annealed structure Cu/La$_2$O$_3$ for photocatalytic application under sunlight

C. Bilel[1] · R. Jbeli[2] · I. Ben Jemaa[3] · A. Boukhachem[4] · F. Saadallah[2] · M. Amlouk[4] · H. Ezzaouïa[2]

Abstract

This paper deals with the synthesis of Cu/La$_2$O$_3$ thin layers and the effect of their surface defects in the photocatalysis process. First, La$_2$O$_3$ thin layers were obtained using pyrolysis technique by spraying at 460 °C on glass substrates. Then, 10 nm thick of Cu is deposited on the top of La$_2$O$_3$ layers by the thermal evaporation process. Finally, these layers are subjected to a heat treatment under air. In order to identify their structures and morphological properties, these layers were characterized by X-ray diffraction, Raman spectroscopy and scanning electron microscope. The optical and electrical properties of these layers were examined using photoluminescence and conductivity measurements, respectively. In addition, the photocatalytic activities of La$_2$O$_3$:Cu thin films were studied by monitoring the degradation of aqueous methylene blue under solar irradiation. It was found that the layer annealed for 2 h exhibited the highest photocatalytic activity. This fact can be explained by the enhancement of its structural and morphological properties.

1 Introduction

Today, the environmental pollution and the energy scarcity are among the world's greatest challenges. The significant progress of the global industrialization has become a major reason to seek a solution to reduce industrial pollution. To solve this problem, various processing technologies are highly developed and subsequently the study of the photocatalytic behavior of various semiconductor oxides has attracted great interest. Many researches are focusing on purifying water from organic contaminants that are an important part of nature. Nowadays, in the photocatalysis field semiconductor is a "Green technology," and it is a potential solution for waste water treatment [1, 2]. The photocatalysis protocol is an effective technology that leads to the degradation of variety of pollutants without selectivity due to the advantages of small size, low cost and good reversibility and simple operation [3–5]. In addition, many semiconductor oxides have become the potential candidate for photocatalytic applications. Oxides have been tested in the photocatalysis. In particular, TiO$_2$ is known as among the most promising material in the field of photocatalysis-based semiconductors. Up to now, according to the literature reviews, there have been a few initiatives to date regarding the use of lanthanum oxide (La$_2$O$_3$) thin films in photocatalytic applications. However, the rapid recombination of photogenerated charge carriers in La$_2$O$_3$ tends to reduce the photocatalytic efficiency [6] and slows down its photocatalytic activity. Currently, the photocatalysts use sunlight instead of other sources of irradiation and therefore enhance the charge separation [7]. Several strategies are developed to improve the charge separation efficiency [8–10]. The doping process is a prospective way to vary the forbidden gap of La$_2$O$_3$ by creating intervening energy levels. This fact improves the charge splitting in order to use the full solar energy and ameliorates the deterioration of dyes molecules in aqueous

✉ C. Bilel
chakroun@ju.edu.sa

✉ R. Jbeli
jbeli.rabi3a@gmail.com

1   Physics Department, College of Science, Jouf University, P.O. Box 2014, Sakaka, Saudi Arabia

2   Laboratoire de Semi-conducteurs, Nanostructures et Technologies Avancées, Centre National de Recherches en Sciences Des Matériaux, B.P. 95, 2050 Hammam-Lif, Tunisia

3   Laboratoire de Photovoltaïque et Matériaux Semi-conducteurs, Université de Tunis El Manar, 1002 Tunis, Tunisia

4   Unité de Physique des Dispositifs à Semiconducteurs, Faculté des Sciences de Tunis, Tunis El Manar University, Tunis, Tunisia

solutions. Many metals and non-metals have been used to narrow the band gap energy of semiconductor oxides.

The main idea of this work is the mobility of monovalent elements such as copper and silver to integrate in thin films of semiconductors under temperature gradient. This property was already exploited in previous works [11, 12]. The binary oxide of La_2O_3 had a large gap, so its use in the photocatalysis domain is limited. It is well interesting to use copper doping element to improve its photocatalytic efficiency. In this context, we synthesized undoped and copper-doped La_2O_3 thin films. Different techniques such as XRD, Raman technique, scanning electron microscopy, PL, and electrical conductivity are used in order to study the influence of Cu doping on structural, optical and electrical properties of Lanthanum oxide. Finally, Cu-doped La_2O_3 thin copper layers tested as high-power materials to decompose the methylene blue (MB) dye under solar irradiation.

2 Materials and methods

2.1 La_2O_3:Cu film synthesis

The films were prepared by dissolving 0.1 M lanthanum chloride ($LaCl_3 \cdot 7H_2O$) in 100 ml of deionized water. The final solution was sprayed on glass substrates at a temperature of 450 °C. This solution flow rate is approximately 4 ml/min through a 0.5-mm-diameter nozzle. Nitrogen was used as a carrier gas and the distance between the nozzle and the substrate was approximately 27 cm [13]. For the preparation of the Cu/La_2O_3 structure, a high purity Cu (Aldrich, 99.9%) was deposited by thermal evaporation (Fig. 1). The metallic copper was placed on a tantalum filament baked in an oven, and then vacuumed to a pressure of 4.8×10^{-6} mbar and a current was applied to the crucibles for 2 min to evaporate the solid 110 variac ($I = 150$ A). After depositing 10 nm of copper on the surface of La_2O_3, the Cu/La_2O_3 bilayers were annealed at different times 0.60, 120, 180 min in air at a temperature of 500 °C in a programmable furnace.

2.2 Characterization technique

First, the structure of the prepared films was obtained using an X-ray machine (Analytical X-Pert PROMPD) and monochromatic radiation CuKα with the wavelength $\lambda = 1.54056$ Å. Secondly, Raman spectroscopy was recorded at room temperature using a Jobin Yvon HR LabRAM in a co-focal backscattering configuration with a spatial resolution of 1 μm and a spectral resolution of less than 0.35 cm^{-1}. The light excitation is an Ar + laser at a wavelength of 488 nm. Additionally, the scanning electron microscope is used to determinate morphological observations of all the films. The photoluminescence spectra were obtained at room temperature in the spectral range of 300–900 nm using a Perkin-Elmer LS 55 fluorescence spectrometer with an excitation radiation of 220 nm.

The electrical properties of La_2O_3:Cu thin copper layers have been determined using an automatically controlled HP4192A analyzer. Electrical measurements were made by two electrodes. These silver paste electrodes were painted on both ends of the sample to avoid a possible diffusion of the silver element into the thin layer. Electrical measurements were limited to 500 °C. These measurements were performed at a temperature between 290 and 370 K and at frequencies between 5 Hz and 13 MHz using an impedance analyzer (type: Hewlett–Packard HP 4192).

The photocatalytic performance of La_2O_3:Cu thin layers deposited on a 2 cm^2 glass substrate placed in a quartz beaker containing 30 ml of 3×10^{-3} M aqueous methylene blue solution was estimated by measuring the decomposition rate of methylene blue (MB) in this aqueous solution under solar radiation in May at a temperature of about 26 °C. The mixture was placed for 30 min in the darkness to obtain the adsorption–desorption equilibrium on the photocatalyst and the methylene blue solution.

The photocatalytic decomposition was estimated by measuring the absorbance of the MB solution in the wavelength range of 400–800 after 0, 60, 120, 180 min of suspension. The variation in MB concentration was determined from the measurement of absorbance solution using the Schimadzu UV 3100 spectrophotometer.

3 Results and interpretations

3.1 Structural properties

XRD patterns of undoped and Cu-doped La_2O_3 thin films annealed at 500 °C in air are shown in Fig. 2. It is important to note that the XRD of undoped and doped films indicated the presence of hexagonal and cubic structure belonging to JCPDS no: 01–083-1345 and JCPDS no: 03–065-3185 boards, respectively. It is found that (001), (100), (011), (012) and (110) peaks are indexed to hexagonal phase of
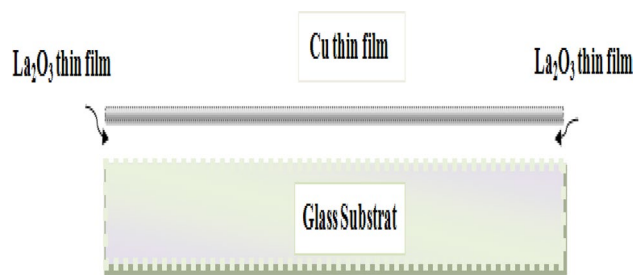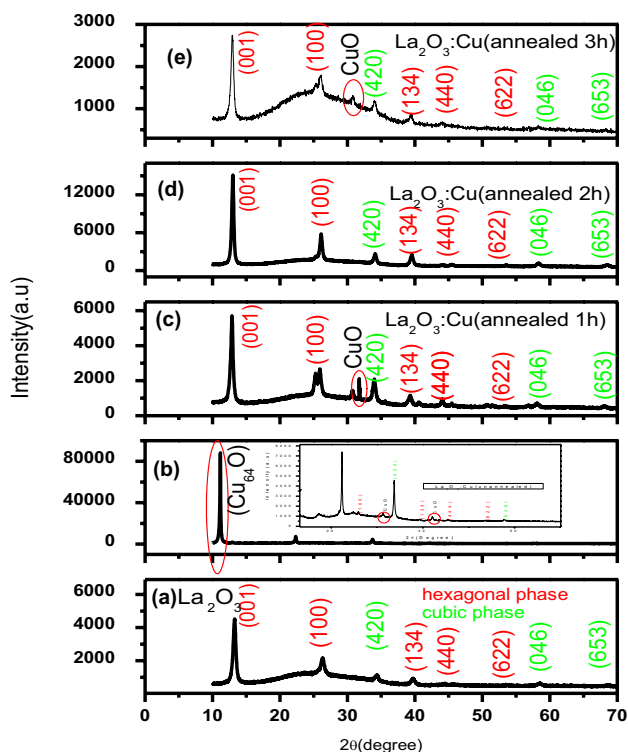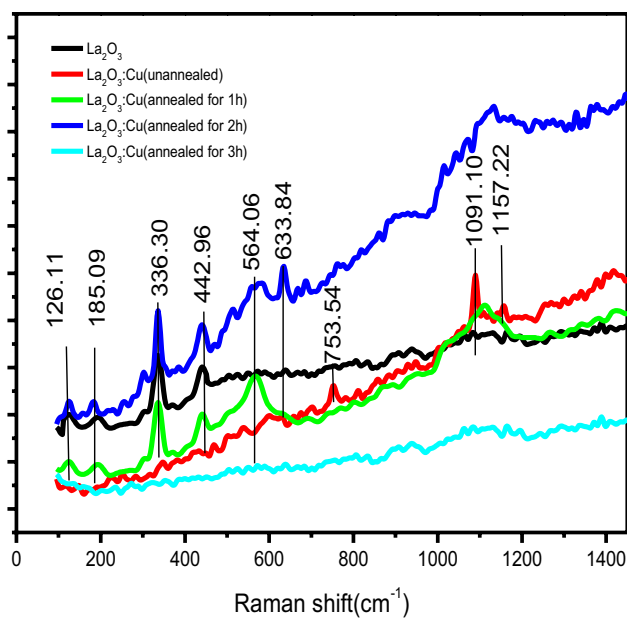

Fig. 1 Configuration of Cu/La_2O_3 thin-film structure

Fig. 2 X-ray diffractograms of **a** La_2O_3, **b** La_2O_3:Cu (unannealed), **c** La_2O_3:Cu (annealed 1 h), **d** La_2O_3:Cu (annealed 2 h), **e** La_2O_3:Cu (annealed 3 h)

Fig. 3 Raman spectra of La_2O_3, La_2O_3:Cu (unannealed), La_2O_3:Cu (annealed 1 h), La_2O_3:Cu (annealed 2 h), La_2O_3:Cu (annealed 3 h)

La_2O_3 and (420), (046), (653) peaks rather satisfied the cubic phase. A preferred orientation along the direction (001) corresponding the hexagonal phase is observed. However, it is interesting to note that copper doping causes a shift from the main peak to the low angles with the appearance of new CuO-related peaks (JCPDS no: 00-44-0706) positioned at 33.72° and 42.11° of low intensity. For the La_2O_3:Cu layer (unannealing), the copper oxide screens the La_2O_3 layer. This is confirmed by the presence a few peaks corresponding to lanthanum oxide. Indeed, the XRD spectrum shows a single intense peak positioned at 11.15° corresponding to the $Cu_{64}O$ phase (JCPDS No. 01-77-1898). This peak disappears completely after the heat treatment. This behavior shows that the increase in temperature during annealing allows the copper atoms to infiltrate into the lanthanum oxide layer, which consequently becomes doped. The main peak of La_2O_3 undergoes a shift after annealing (Fig. 2b) indicating a modification of the structure by the incorporation of Cu atoms in the crystalline mesh.

On the other hand, a lot of information on microstructure and lattice defects is provided by Raman spectroscopy. Figure 3 depicts Raman spectra of Cu-doped La_2O_3 thin films. Four broad bands located at 126.11, 185.05, 336.19 and 442.52 cm^{-1} are seen. At a first glance, an intense peak located at 336.19 cm^{-1} corresponds to La–O vibration,

which is previously reported by Cui et al. [14]. In the same line, the two bands assigned at 126.11 and 185.05 cm^{-1} are related to cubic and hexagonal varieties, respectively, [15] which are consistent with XRD analysis. The band at 442.52 cm^{-1} corresponds to Eg $\nu1$ mode [16]. After doping with copper and before annealing, these bands disappeared and it is important to note that the apparition of a band situated at 1091.10 cm^{-1} can be allocated to multi-phonon transition of Cu–O [17]. After the annealing process for 1 h and 2 h, the four bands recurred with the apparition of another peak situated at 564.06 cm^{-1} which corresponds to the B_{2g} mode of CuO. Figure 4a–d shows the surface area observed by SEM of undoped and Cu-doped La_2O_3 thin films. The surfaces of undoped and Cu-doped La_2O_3 thin films are rough. These surfaces are characterized by small crystals which have developed separately and are fused to chains with different lengths. The identical morphology is seen with silver-doped La_2O_3 thin films [18].

3.2 Fourier transform infrared spectroscopy (FTIR)

FTIR spectroscopy is a high-powered technique parallel to X-ray diffraction analysis to examine the structural defects of semiconductor materials by the acknowledgment of the different types of bonds between atoms. In this work, the FTIR analysis is carried out in the wave number ranging from 400 to 5000 cm^{-1}. Figure 5 shows the FTIR spectra of La_2O_3 and La_2O_3:Cu. It was observed that an infrared peak located at 457 cm^{-1} is related to La–O vibration which confirms the presence of La_2O_3 material [19].

Fig. 4 SEM images of: **a** pure La$_2$O$_3$, **b** La$_2$O$_3$:Cu (unannealed), **c** La$_2$O$_3$:Cu (annealed 2 h) and **d** La$_2$O$_3$:Cu (annealed 3 h). **e** Evolution of grain size with annealing time
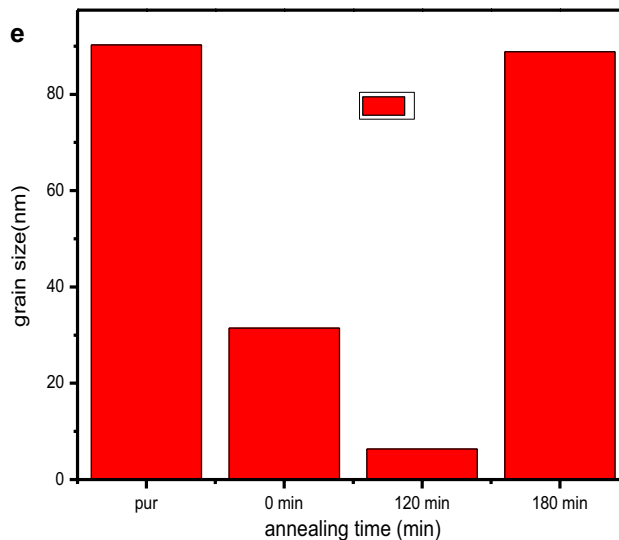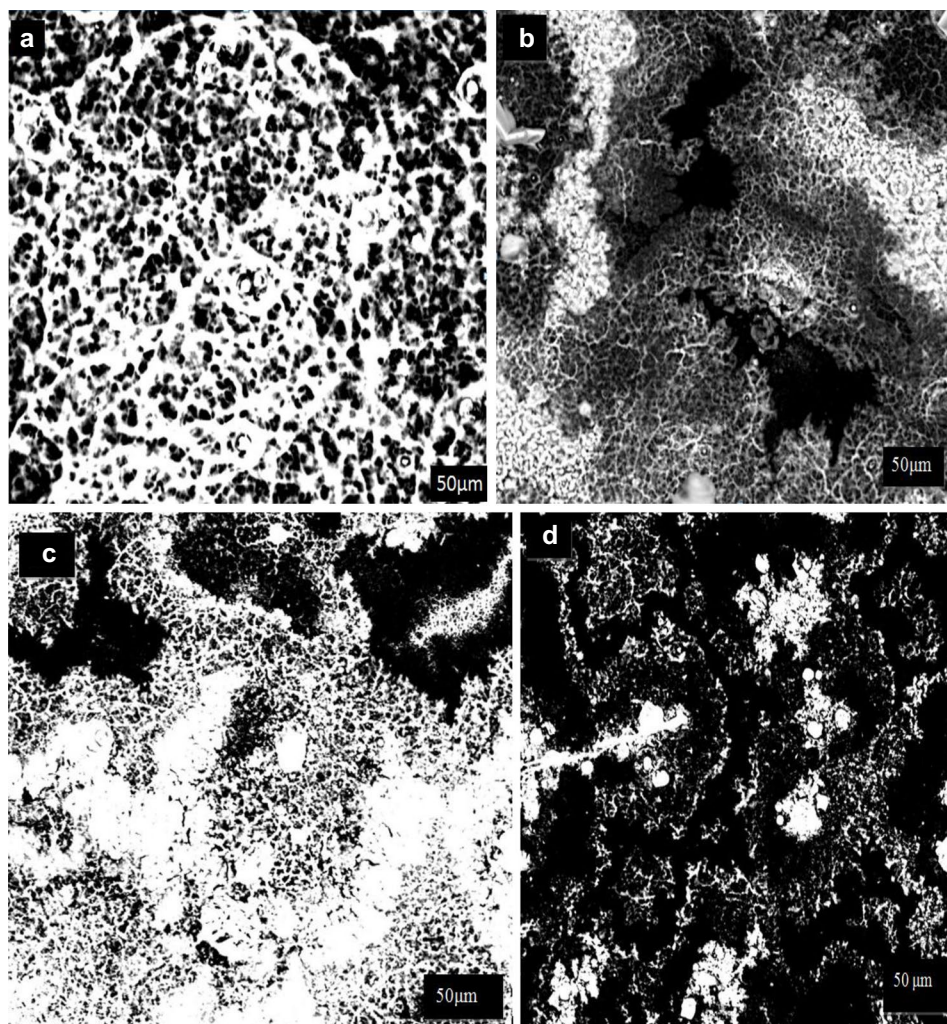
Furthermore, a medium band appears at 752 cm^{-1} and is linked to C–Cl. A strong peak is situated at 1054 cm^{-1} that can be attributed to C=O bonding. The narrow absorption peak observed around at 1221 cm^{-1} can be ascribed to the weight loss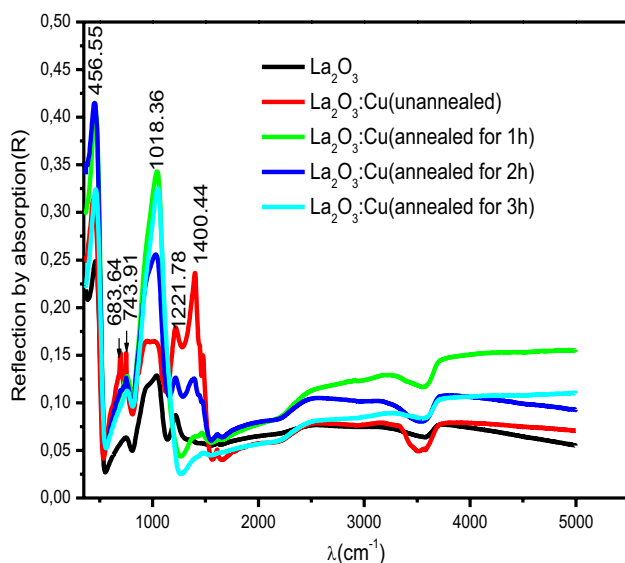 of the La$_2$O$_3$ nanoparticles [20]. The peak at 1400 cm^{-1} corresponds to the well-known ν3 stretching vibration of the carbonate group [21].

It is worth noting that new peak observed in the FTIR spectra of Cu-doped La_2O_3 films around 683.64 cm^{-1} may be related to CuO. This is in accordance with the X-ray diffraction analysis outline above.

3.3 Optical properties

The photoluminescence (PL) is a powerful optical technique that gives further information on the energy states concerning defects and impurities inside a material. All PL measurements were carried out in 200 to 900 nm wavelength domain using 220 nm as excitation wavelength. All the spectra display two emission peaks towards 423 nm and 484 nm positions, with similar curve shapes which are attributed to visible emission showing that doping with copper does not lead to new PL emissions. Figure 6 shows a significant shift of peak position towards longer wavelength compared to undoped La_2O_3. This behavior may be explained by the change in the optical band gap (narrowing) of the material [22] and confirms the doping states in La_2O_3 lattice. This result can support the enhancement of photocatalytic efficiency described below. The same figure indicates a quenching of PL intensities. The last depends mainly on the presence of Cu and the heat treatment process. In fact, the increase of the annealing time causes a recombination inhibition which can be explaining by an increase of defects density in the band gap as well as the trapping.

The Gaussian deconvolution of both undoped and Cu-doped La_2O_3 layers is shown in Fig. 7. At the beginning, the spectra keep the same emission peaks and all the emission peaks are in the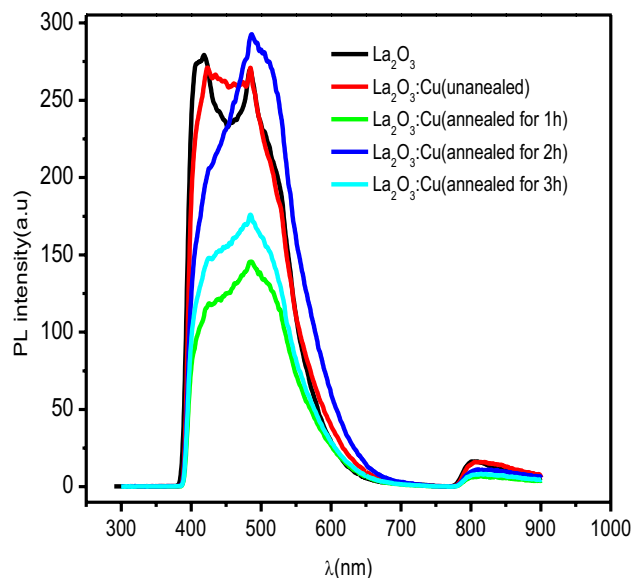 visible range. These peaks are mainly linked to electronic states related to the intrinsic defects in La_2O_3 localized in the band gap of La_2O_3 material [23]. Generally, the most common defects that cause visible oxide emission are the oxygen vacancies. The lanthanum oxide or lanthanum sulfide nanobelts are known by the green luminescence mechanism. This emission is set at 500–560 nm, and it can be linked to the transition of electrons from the deep oxygen vacuum level to the top of the valence band [24]. It should be pointed out that the presence of copper slows the radiative recombination's process, and causes a low recombination of photogenerated charge carriers, which will be beneficial for possible sensitivity applications [25].

3.4 Electrical properties

The electrical responses of Cu-doped La_2O_3 thin films were studied using the complex impedance technique in a wide frequency range from 100 Hz to 13 MHz and at temperatures between 460 and 540 °C with a pitch of 10 °C. The Nyquist (Z'' vs Z') extracted from the impedance spectroscopy measurements is given in Fig. 8a–d. However, these traces are made up of a semicircle offset from the origin and are not centralized on the real axis. Their radius decreases with rising temperature because of the different dipole types present in the material. These dipoles are marked by their own relaxation time which leads to multi-relaxation processes [26]. In addition, Fig. 9a–d shows the plot of the imaginary part Z'' as a function of frequency at different temperatures that increase monotonously with increasing frequency. These curves are characterized by a maximum peak at a particular

Fig. 5 FTIR spectrum of La_2O_3, La_2O_3:Cu (unannealed), La_2O_3:Cu (annealed in air for 1 h), La_2O_3:Cu (annealed in air for 2 h), La_2O_3:Cu (annealed in air for 3 h)

Fig. 6 PL spectra of La_2O_3, La_2O_3:Cu (unannealed), La_2O_3:Cu (annealed in air for 1 h), La_2O_3:Ag (annealed in air for 2 h) and La_2O_3:Ag (annealed in air for 3 h)
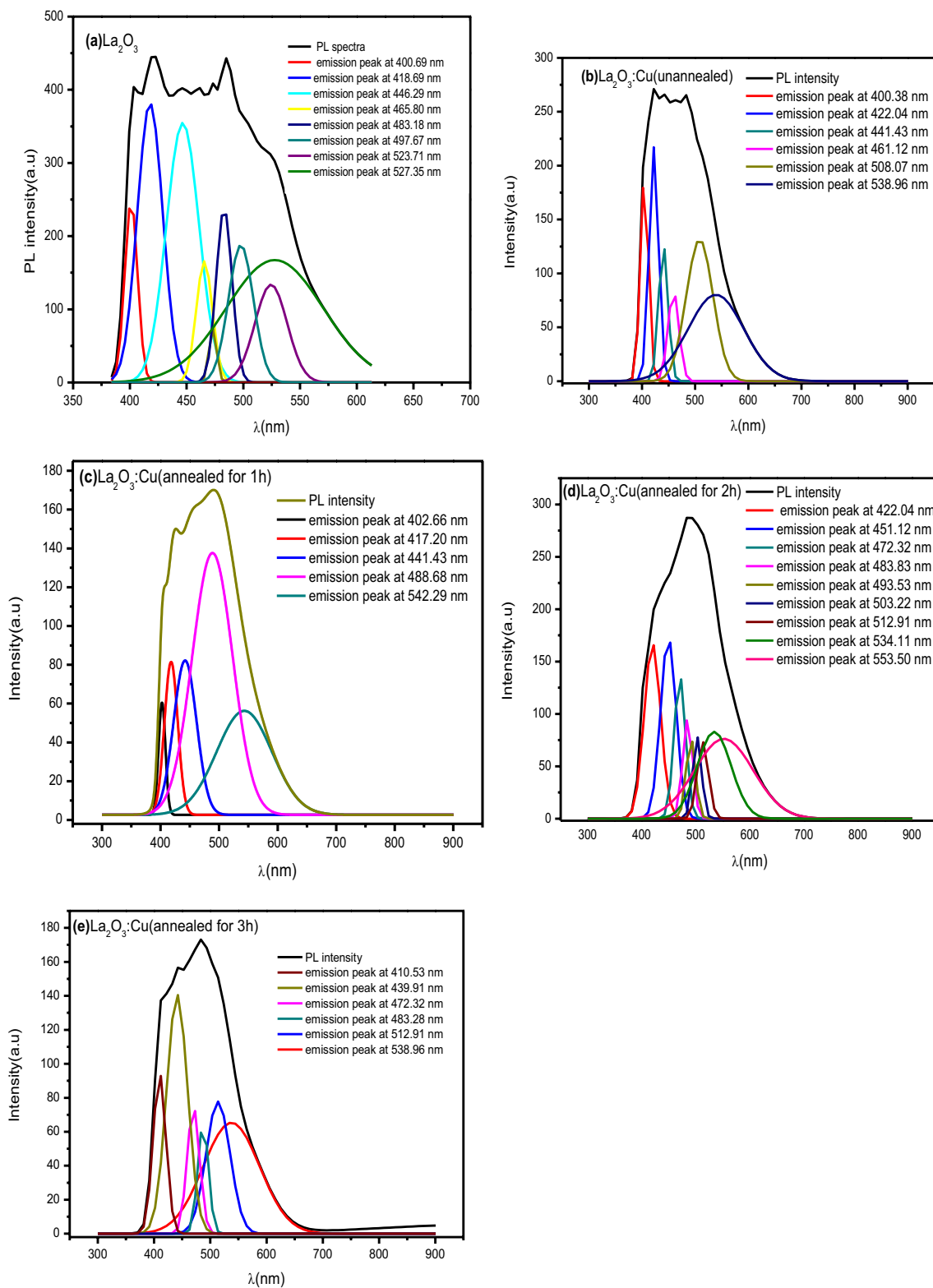
Fig. 7 Deconvoluted with Gaussian curves of **a** La$_2$O$_3$, **b** La$_2$O$_3$:Cu (unannealed), **c** La$_2$O$_3$:Cu (annealed 1h), **d** La$_2$O$_3$:Cu (annealed 2h), **e** La$_2$O$_3$: Cu (annealed 3h)
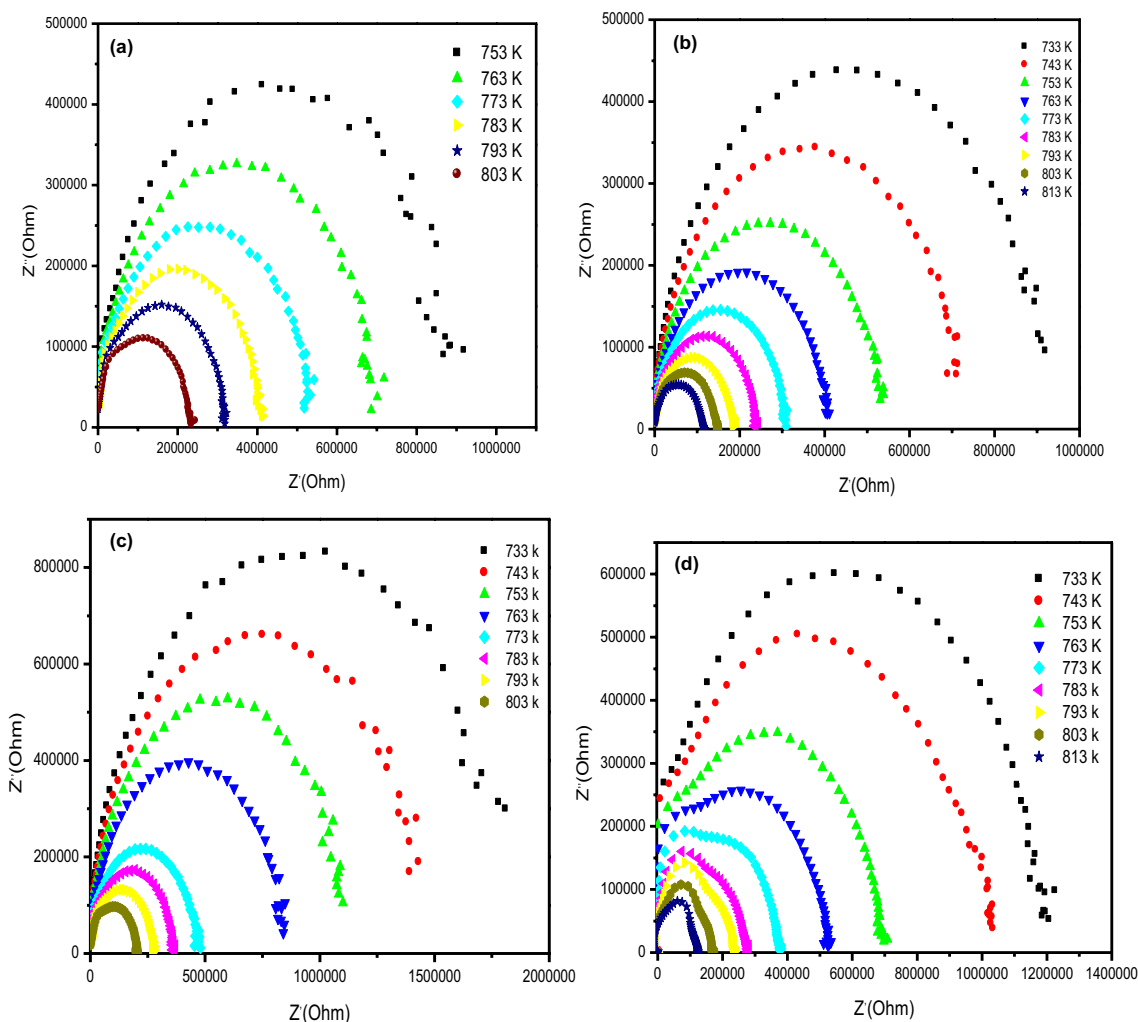
Fig. 8 Complex impedance spectra of **a** La$_2$O$_3$, **b** La$_2$O$_3$:Cu (annealed for 1 h), **c** La$_2$O$_3$:Cu (annealed for 2 h) and **d** La$_2$O$_3$:Cu (annealed for 3 h) thin films

frequency. This peak has a tendency to move towards high frequencies with an asymmetrical expansion suggesting the existence of a distributed relaxation process [27]. The maximum values of Z'' provide the relaxation frequencies which are regulated by Arrhenius' law (Eq. 1):

$$f_{max} = f_0 e^{-\frac{E_{a(Z'')}}{k_B T}}, \tag{1}$$

where $E_{a(Z'')}$ is the activation energy, and f_0 is a distinctive frequency expressed by $2\pi f_0 \tau = 1$ where τ is the characteristic relaxation time of the phonons.

The fit of the Ln (f_{max}) vs ($1000/T$) (as seen in Fig. 10) leads to the calculation of the activation energies $E_{a(Z'')}$ which are recapitulated in Table 1. The decrease in activation energy values with Cu doping may be due to the increase in the thermally activated hopping rate process [28]. From Fig. 10, the values $E_{a(Z'')}$ for La$_2$O$_3$:Cu annealed for 3 h are

equal to 1.88 eV for low temperature and 0.36 eV for high temperature. This is dependent on a possible change in stoichiometry. The possibility of oxygen incorporation is increased under air atmosphere and at high temperature. A modification of the electrical characteristics is cited in the obtained thin film. The global conductivity of the films can be governed by Jonscher's law of universal power [29] (Eq. 2):

$$\sigma_t = \sigma_{DC} + \sigma_{AC}(T, \omega) = A\omega^s, \tag{2}$$

where A is a constant and s is the power exponent.

In order to determine the transport mechanism of the samples, AC conductivity measurements were extensively studied. Figure 11 shows the slope of $\ln(\sigma_t)$ against $\ln(\omega)$. From the curves, it is clear that electrical conduction is improved in films by a jump of polarons between adjacent sites [30]. Figure 12 displays the evolution of the
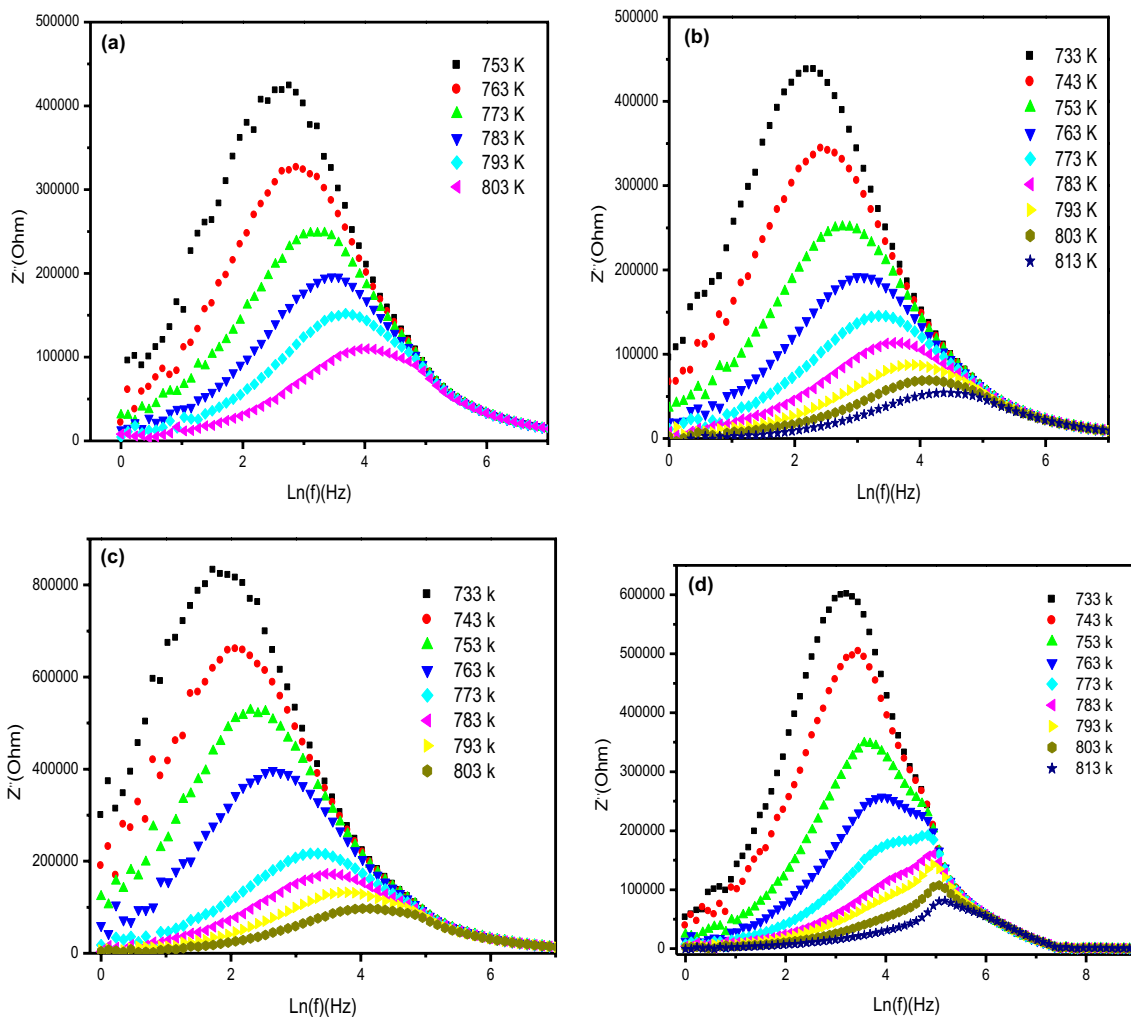
Fig. 9 Angular frequency dependence of Z'' of **a** La$_2$O$_3$, **b** La$_2$O$_3$:Cu (annealed 1 h), **c** La$_2$O$_3$:Cu (annealed 2 h) and **d** La$_2$O$_3$:Cu (annealed 3 h)
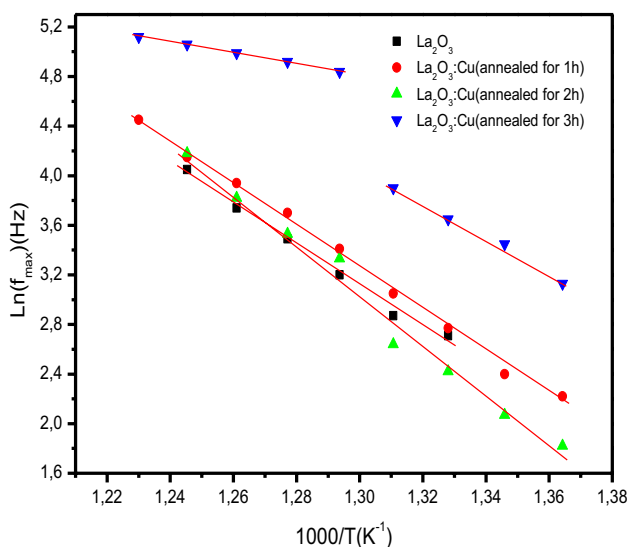

Fig. 10 Plot of ln $f_{\max_{(Z'')}}$ versus $1000/T$

Table 1 Some electrical parameters of the Cu-doped La$_2$O$_3$ thin films

	$E_{a_{(Z'')}}$ (eV)	$E_{a(DC)}$ (eV)	ω_m (eV)
Pure La$_2$O$_3$	1.41	1.46	1.72
La$_2$O$_3$:Cu (annealed for 1 h)	1.47	1.4	1.66
La$_2$O$_3$:Cu (annealed for 2 h)	1.76	1.71	1.78
La$_2$O$_3$:Cu (annealed for 3 h)	1.88	1.53	–
	0.36	–	–

frequency exponent s with temperature. This parameter decreases linearly with temperature rising. This highlights the fact that charge carriers in Cu-doped La$_2$O$_3$ thin layers are guided by the CBH model as the predominant charge transport mechanism in which charge carriers jump between sites over a potential barrier that splits them [31]. According to this model, the angular frequency exponent s is bound to temperature by the following expression [32, 33] (Eq. 3):
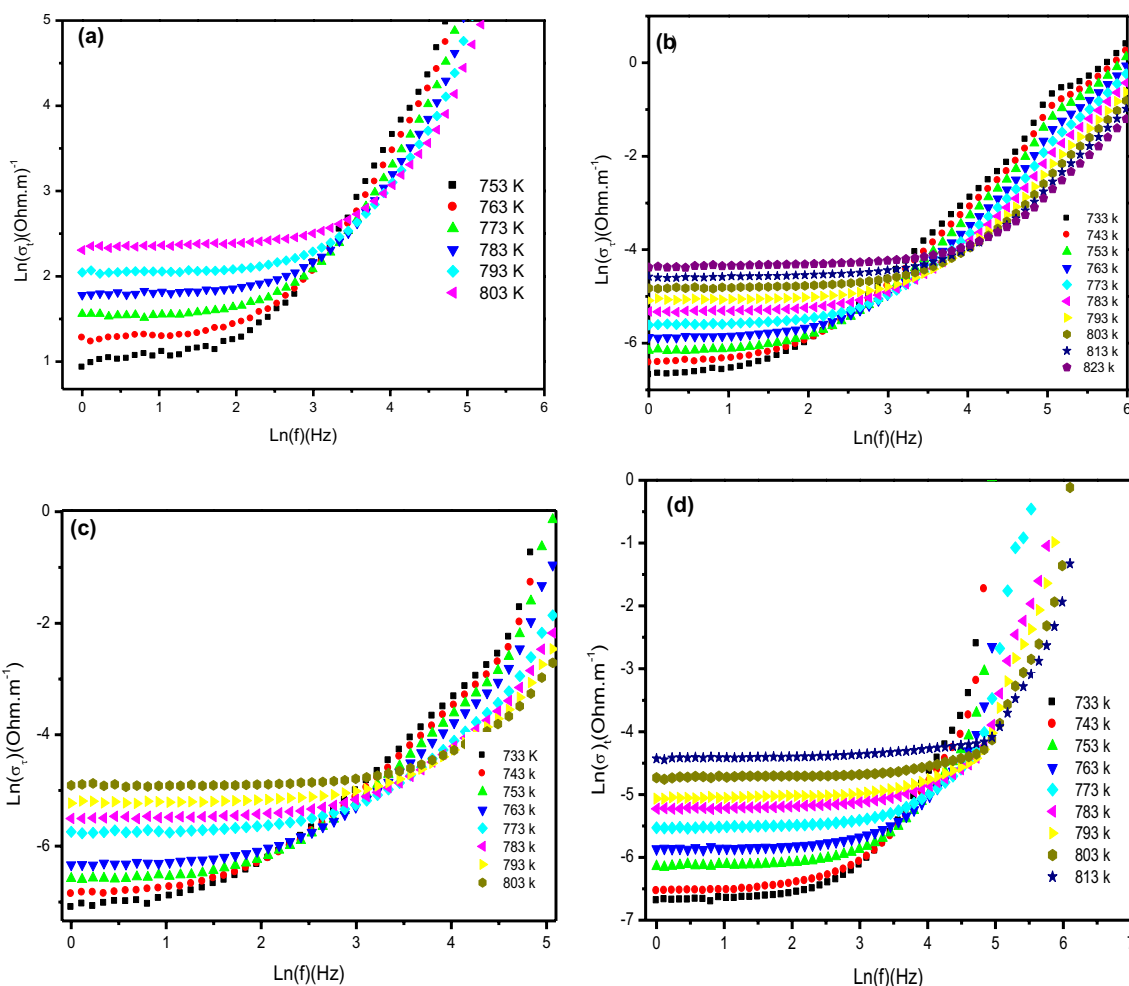
Fig. 11 Angular frequency dependence of AC conductivity of **a** La$_2$O$_3$, **b** La$_2$O$_3$:Cu (annealed 1 h), **c** La$_2$O$_3$:Cu (annealed 2 h), **d** La$_2$O$_3$:Cu (annealed 3 h) thin films
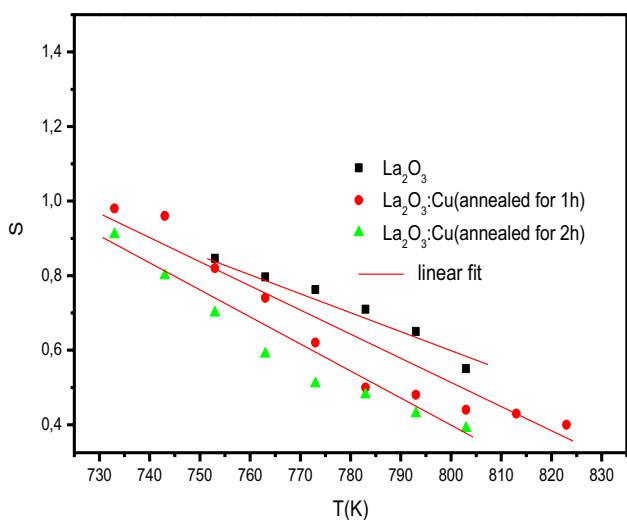
Fig. 12 Plot of *S* versus *T*

$$s = 1 - \frac{6k_{\mathrm{B}}T}{\omega_{\mathrm{m}}}, \tag{3}$$

where ω_m is the difference between the bipolaron level and the conduction band energy. The variation of the slope of *s* as a function of the temperature (Fig. 12) allows us to obtain ω_{m} value, which is recapitulated in Table 1. From the above results, it can be seen that the maximum barrier height (ω_{m}) is decreasing slowly by raising annealing time up to 1.66 (eV), and it rises slowly. The DC conductivity data were analyzed using the Arrhenius law [34] (Eq. 4):

$$\sigma_{\mathrm{DC}} = \frac{C}{T}e^{-\frac{E_{\mathrm{a(DC)}}}{k_{\mathrm{B}}T}}. \tag{4}$$

Figure 13 shows the variation of $\ln(\sigma_{\mathrm{DC}} \cdot T)$ vs $1000/T$. The increase of DC conductivity in term of temperature is originated from a thermally activated process. This phenomenon can be interpreted by the semiconductor attitude of these Cu-doped La$_2$O$_3$-sprayed thin films. In the first part, the values
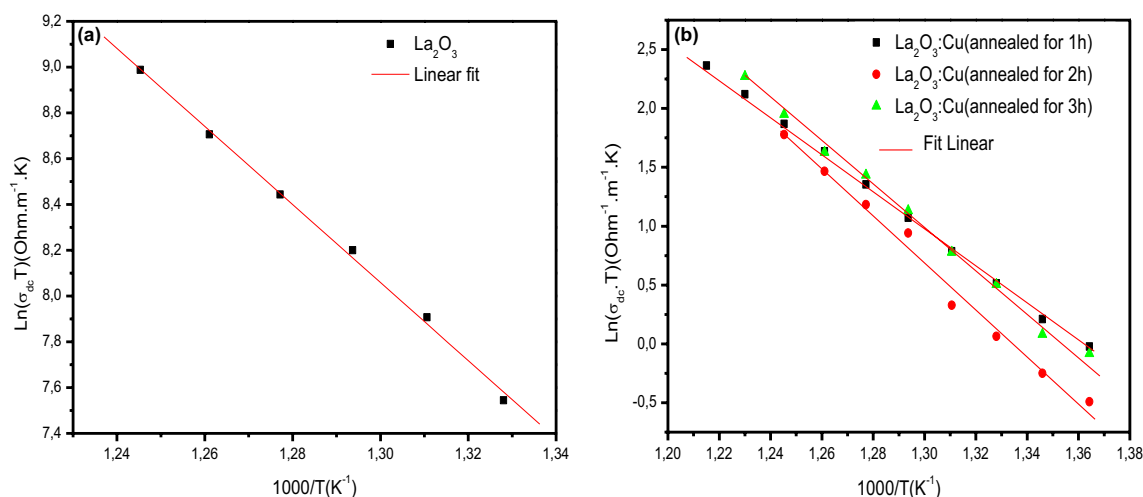
Fig. 13 Temperature dependence of the parameters **a** pure La$_2$O$_3$, **b** La$_2$O$_3$: Cu (annealed at different time)

of E_a are determined using the Eq. 1. In the second part, $E_{a(DC)}$ is calculated via the slope of $\ln(\sigma_{DC} \cdot T)$ against the inverse of temperature. The values obtained from Eq. 4 are summarized in Table 1. It is important to note that these values are very close with those deduced from the relaxation frequency which confirms the hopping conduction process [35]. The result of the jump frequency and conductivity of the direct current leads to the conclusion that the conduction pathway is linked to a similar transport mechanism.

3.5 Photocatalytic activity

From the structural investigations described above, it is worth noting that after an annealing process under air, the structures based on Cu/La$_2$O$_3$ thin films seem to be as nanocomposites formed by a mixture between CuO and La$_2$O$_3$ materials. The proportion between the two phases is substantially less than 10% (CuO/La$_2$O$_3$ ratio < 10%) because the CuO oxide does not appear as an apparent phase during the X-ray diffraction analysis. It is for this reason that the designation of these structures has been maintained as doped thin films. The photocatalytic activity of such structures was tested for the first time to degrade MB dye under sunlight although only La$_2$O$_3$ thin-film material having a wide gap energy is not able to accomplish this photocatalytic power in visible range. Indeed, the monitoring of the absorbance of maximum band of MB ($\lambda = 665$ nm) is a manner of controlling the photocatalytic effect of such structures. Figure 14a shows the time evolution of spectral variations during the decomposition of the MB aqueous solution mediated by La$_2$O$_3$ and La$_2$O$_3$:Cu thin films under sunlight after exposure for 3 h. The degradation of this dye is difficult in the absence of the catalysts and the autodegradation of this dye is negligible. On the contrary, as seen in Fig. 14a, the photocatalytic activity is significantly enhanced and the deterioration

of MB compounds is almost total for copper-doped La$_2$O$_3$ thin films after irradiation for three hours as compared to undoped thin film. Generally, the improvement in photocatalytic activity strongly depends on many factors, like crystallinity, optical properties and the surface state as well as the absorption properties [36]. The enhanced photocatalytic activity can be interpreted by the strongly dependence on the surface state of the films [37]. It is well known that the decrease in the grain size and the surface roughness (large specific surface) leads to an increase in the photocatalytic activity. For this context, SEM observation of La$_2$O$_3$:Cu (annealed for 2 h) indicates that the grain size is smaller than the other samples. The same behavior has been observed by Yunjian Wang [38]. Indeed, the decrease of grain size of the SrMoO$_4$:Bi^{3+} in comparison with the pure SrMoO$_4$ leads to a great improvement in photocatalytic activity.

As well, Fig. 4e shows the calculation of grain size using Image *J* software, which proves the previous observations. The enhanced photocatalytic activity was achieved due the copper doping which reinforces the appearance of the trapping centers. In fact, the presence of copper with the heat treatment results in the generation of trap levels in the prohibited band of lanthanum oxide. Both the oxygen vacancies and oxygen interstitials play a vital role in photodegradation process by minimizing the recombinant process of electron–hole pairs [39, 40]. It can also be observed that the photocatalytic degradation of a dye follows the pseudo-first-order kinetics [41, 42] (Eq. 5):

$$\ln\left(\frac{C}{C_0}\right) = -kt. \tag{5}$$

The plot of $\ln(C_0/C)$ versus time intervals (Fig. 14b) allows to calculate directly the values of k in which C^0 and
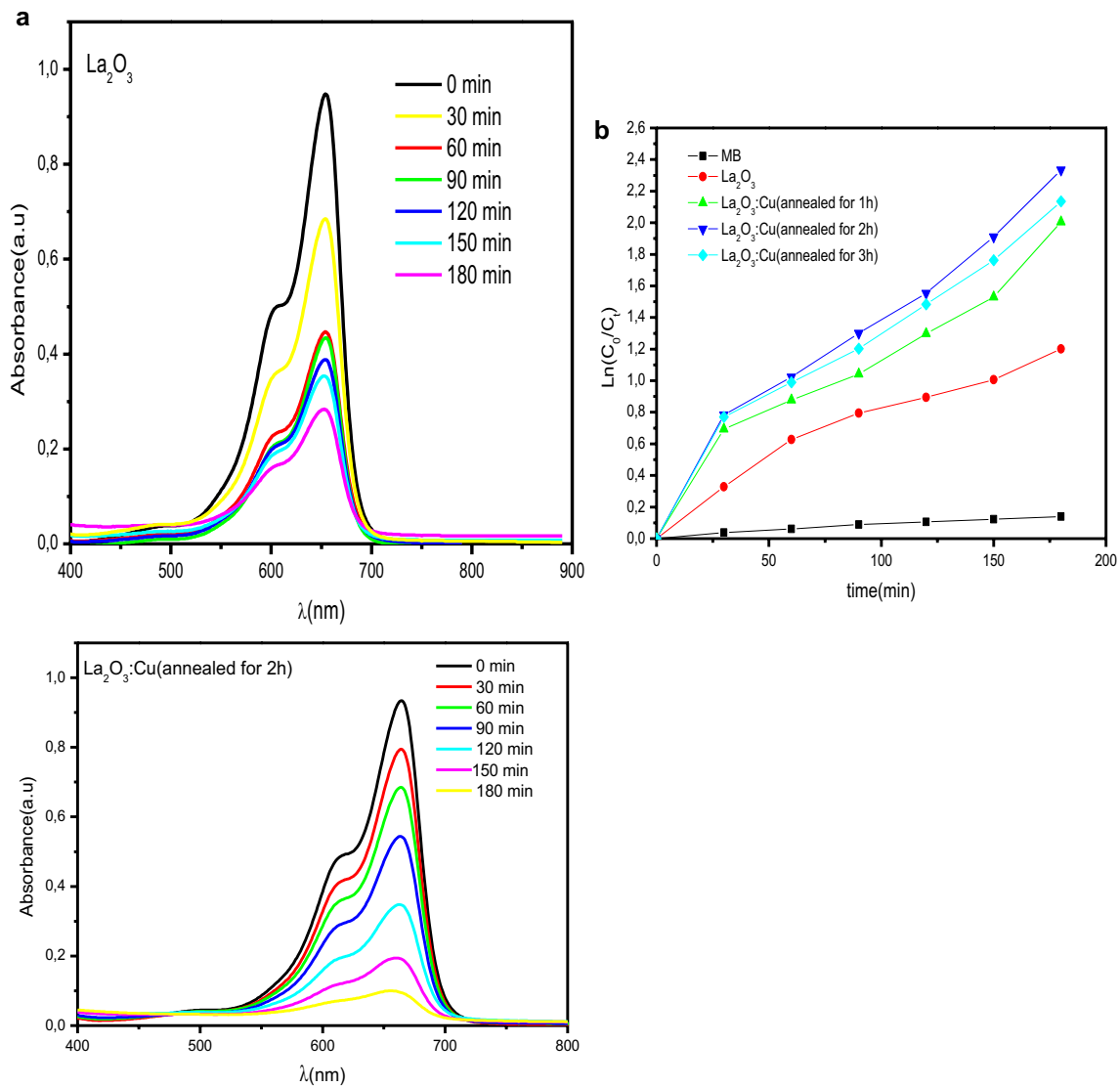
Fig. 14 **a** Time-dependent absorption spectra of MB solution under sunlight irradiation in the presence of undoped La_2O_3 and La_2O_3:Cu (annealed for 2 h) thin films. **b** Photocatalytic degradation kinetics of MB dye for Cu-doped La_2O_3 thin films

Table 2 Kinetic parameter of Cu-doped La_2O_3 thin films for MB dye

Sample	Rate constant, K (10^{-3} min^{-1})
MB	0.75
Pure La_2O_3	6.2
La_2O_3:Cu (annealed for 1 h)	9.6
La_2O_3:Cu (annealed for 2 h)	11.66
La_2O_3:Cu (annealed for 3 h)	10.57

C denote the dye concentration at $t = 0$ and t, respectively, after the equilibrium adsorption. Table 2 summarizes the values of the kinetic rate determinate from the slope of the adjusted curves. It is found that the kinetic of the first-order

degradation rate constants passes from $k = 6.2 \times 10^{-3}$ min^{-1} for pure La_2O_3 to $k = 11.66 \times 10^{-3}$ min^{-1} k for La_2O_3:Cu annealed for 2 h, respectively.

4 Conclusion

Cu-doped La_2O_3 thin layers were synthesized by the both technique spray pyrolysis and thermal evaporation. Many techniques are used to analyze their physical properties. XRD study indicates a mixture of hexagonal and cubic phase with crystallites oriented along (001) direction. Besides, the addition of copper leads to appearance of secondary phase of CuO. The interpretation of the Raman and FTIR spectra shows the existence of La_2O_3 variety. Moreover, the

photoluminescence (PL) measurement indicates that the presence of copper decreases the PL intensity. The study of the electrical conduction mechanism inside a thin film displays that the charge carrier jumps between localized states in the band gap are responsible for conduction. It was found that the obtained Cu/La_2O_3 structure is suitable for the photocatalytic application. Finally, the optimal activity was obtained when the sample was annealed for 2 h.

References

1. S. Dong, J. Feng, M. Fan, Y. Pi, L. Hu, X. Han, M. Liu, J. Sun, J. Sun, Recent developments in heterogeneous photocatalytic water treatment using visible light responsive photocatalysts: a review. RSC Adv. **5**, 14610–14630 (2015)

2. L. Jing, W. Zhou, G. Tian, H. Fu, Surface tuning for oxide-based nanomaterials as efficient photocatalysts. Chem. Soc. Rev. **42**, 9509–9549 (2013)

3. D.B. Hernandez-Uresti, D.S. Martinez, A.M. de la Cruz, S.S. Guzman, L.M. Torres-Martinez, Characterization and photocatalytic properties of hexagonal and monoclinic WO_3 prepared via microwave-assisted hydrothermal. Ceram. Int. **40**, 4767–4775 (2014)

4. Y. Guo, X. Quan, N. Lu, H. Zhao, S. Chen, High photocatalytic capability of assembled nanoporous WO_3 with preferential orientation of (002) planes. Environ Sci Technol. **41**, 4422–4427 (2012)

5. A. Ali, X. Zhao, A. Ali, L. Duan, H. Niu, C. Peng, Y. Wang, S. Hou, Enhanced photocatalytic activity of ZnO nanorods grown on Ga doped seed layer. Superlattices Microstruct. **83**, 422–430 (2015)

6. M.N. Chong, B. Jin, C.W. Chow, C. Saint, Recent developments in photocatalytic water treatment technology: a review. Water Res. **44**, 2997–3027 (2010)

7. V. Sanna, N. Pala, V. Alzari, D. Nuvoli, M. Carcelli, ZnO nanoparticles with high degradation efficiency of organic dyes under sunlight irradiation. Mater. Lett. **162**, 257–260 (2016)

8. A.A. Dubale, A.G. Tamirat, H.M. Chen, T.A. Berhe, C.J. Pan, W.N. Su, B.J. Hwang, A highly stable CuS and CuS–Pt modified Cu_2O/CuO heterostructure as an efficient photocathode for the hydrogen evolution reaction. J. Mater. Chem. A **4**, 2205–2216 (2016)

9. J. Yu, S. Zhuang, X. Xu, W. Zhu, B. Feng, J. Hu, Photogenerated electron reservoir in hetero-p–n CuO–ZnO nanocomposite device for visible-light driven photocatalytic reduction of aqueous Cr(VI). J. Mater. Chem. A **3**, 1199–1207 (2015)

10. M. Saranya, R. Ramachandran, P. Kollu, S.K. Jeong, A.N. Grace, A template-free facile approach for the synthesis of CuS–rGO nanocomposites towards enhanced photocatalytic reduction of organic contaminants and textile effluents. RSC Adv. **5**, 15831–15840 (2015)

11. A. Amlouk, K. Boubaker, M. Amlouk, A new procedure to prepare semiconducting ternary compounds from binary buffer materials and vacuum-deposited copper for photovoltaic applications. Vacuum **85**, 60–64 (2010)

12. J.C. Bernede, A. Conan, E. Fouesnant, B. El Bouchairi, G. Goureaux, Polarized memory switching effects in $Ag_2Se/Se/M$ thin film sandwiches. Thin Solid Films **97**, 165–171 (1982)

13. C.S. Prajapati, P.P. Sahay, Alcohol-sensing characteristics of spray deposited ZnO nano-particle thin films Sensor. Actuators B **160**, 1043–1049 (2011)

14. J. Cui, G.A. Hope, Raman and fluorescence spectroscopy of CeO_2, Er_2O_3, Nd_2O_3, Tm_2O_3, Yb_2O_3, La_2O_3, and Tb_4O_7. J. Spectrosc. (2015). https://doi.org/10.1155/2015/940172

15. A. Orera, G. Larraz, M.L. Sanjuán, Spectroscopic study of the competition between dehydration and carbonation effects in La_2O_3-based materials. J. Eur. Ceram. Soc. **33**, 2103–2110 (2013)

16. J.H. Denning, S.D. Ross, The vibrational spectra and structures of rare earth oxides in the A modification. J. Phys. C Solid State Phys. **5**, 1123–1133 (1972)

17. R. Shabu, A. Moses Ezhil Raj, C. Sanjeeviraja, C. Ravidhas, Assessment of CuO thin films for its suitability as window absorbing layer in solar cell fabrications. Mater. Res. Bull. **68**, 1–8 (2015)

18. R. Jbeli, A. Boukhachem, I. Ben Jemaa, N. Mahdhi, F. Saadallah, H. Elhouichet, S. Alleg, M. Amlouk, H. Ezzaouïa, An enhancement of photoluminescence property of Ag doped La2O3 thin films at room temperature. Spectrochim. Acta Part A **184**, 71–81 (2017)

19. A.A. Yadav, A.C. Lokhande, C.D. Lokhande, A simple chemical route for synthesis of microrods-like La_2O_3 thin films. Mater. Lett. **160**, 500–502 (2015)

20. K. Bikshalu, V.S.K. Reddy, P.C.S. Reddy, K.V. Rao, Synthesis of La_2O_3 nanoparticles by Pechini method for future CMOS applications. IJEAR **4**, 12–15 (2014)

21. D. Tsoutsou, G. Scarel, A. Debernardi, S.C. Capelli, S.N. Volkos, L. Lamagna, S. Schamm, P.E. Coulon, M. Fanciulli, Infrared spectroscopy and X-ray diffraction studies on the crystallographic evolution of La_2O_3 films upon annealing. Microelectron. Eng. **85**, 2411–2413 (2008)

22. K. Mageshwari, R. Sathyamoorthy, Physical properties of nanocrystalline CuO thin films prepared by the SILAR method. Mater. Sci. Semicond. Process. **16**, 337–343 (2013)

23. C. Hu, H. Liu, W. Dong, Y. Zhang, G. Bao, C. Lao, Z.L. Wang, $La(OH)_3$ and La_2O_3 nanobelts—synthesis and physical properties. Adv. Mater. **19**, 470–474 (2007)

24. P. Chand, A. Gaur, A. Kumar, Structural, optical and ferroelectric behavior of CuO nanostructures synthesized at different pH values. Superlattices Microstruct. **60**, 129–138 (2013)

25. C. Mrabet, M. Ben Amor, A. Boukhachem, M. Amlouk, T. Manoubi, Physical properties of La-doped NiO sprayed thin films for optoelectronic and sensor applications. Ceram. Int. **42**, 5963–5978 (2016)

26. M.M. El-Nahass, H.A.M. Ali, M. Saadeldin, M. Zaghllol, AC conductivity and dielectric properties of bulk tungsten trioxide (WO_3). Phys B **407**, 4453–4457 (2012)

27. T. Nagata, T. Shimura, A. Ashida, N. Fujimura, T. Ito, Electro-optic property of ZnO: X (X = Li, Mg) thin films. J Crystal Growth **237**, 533–537 (2002)

28. A.E. Bekheet, N.A. Hegab, Ac conductivity and dielectric properties of $Ge_{20}Se_{75}In_5$ films. Vacuum **83**, 391–396 (2000)

29. S.S. Kale, K.R. Jadhav, P.S. Patil, T.P. Gujar, C.D. Lokhande, Characterizations of spray-deposited lanthanum oxide (La_2O_3) thin films. Mater. Lett. **59**, 3007–3009 (2005)

30. A.K. Jonscher, The universal dielectric response. Nature **267**, 673 (1977)

31. B. Ouni, M. Haj Lakhdar, R. Boughalmi, T. Larbi, A. Boukhachem, A. Madani, K. Boubaker, M. Amlouk, Investigation of electrical and dielectric properties of antimony oxide (Sb2O4) semiconductor thin films for TCO and optoelectronic applications. J. Non-Cryst. Solids. **367**, 1–7 (2013)

32. M. Haj Lakhdar, B. Ouni, M. Amlouk, Dielectric relaxation, modulus behavior and conduction mechanism in Sb_2S_3 thin films. Mater. Sci. Semicond. Process. **19**, 32–39 (2014)

33. T. Larbi, A. Amara, L. Ben Said, B. Ouni, M. Haj Lakhdar, M. Amlouk, A study of optothermal and AC impedance properties of Cr-doped Mn_3O_4 sprayed thin films. Mater. Res. Bull. **70**, 254–262 (2015)

34. A. Arfaoui, A. Mhamdi, B. Khalfallah, S. Belgacem, M. Amlouk, Physical characterizations of the sprayed $ZrMo_2O_8$ thin films. Appl. Phys A (2019). https://doi.org/10.1007/s00339-019-2818-z

35. R. Boughalmi, A. Boukhachem, M. Kahlaoui, H. Maghraoui, M. Amlouk, Physical investigations on Sb_2S_3 sprayed thin film for optoelectronic applications Mater. Sci. Semicond. Process. **26**, 593–602 (2014)

36. G. Kenanakis, N. Katsarakis, Ultrasonic spray pyrolysis growth of ZnO and ZnO: Al nanostructured films: application to photocatalysis. Mater. Res. Bull. **60**, 752–759 (2014)

37. H. Xu, H. Li, G. Sun, J. Xia, C. Wu, Z. Ye, Q. Zhang, Photocatalytic activity of La_2O_3-modified silver vanadates catalyst for Rhodamine B dye degradation under visible light irradiation. Chem. Eng. J. **160**, 33–41 (2010)

38. Y. Wang, H. Xu, C. Shao, J. Cao, Doping induced grain size reduction and photocatalytic performance enhancement of $SrMoO_4$:Bi^{3+}. Appl. Surf. Sci. **392**, 649–657 (2017)

39. C. Xu, L. Cao, G. Su, W. Liu, X. Qu, Y. Yu, Preparation, characterization and photocatalytic activity of Co-doped ZnO powders. J. Alloys Compd. **497**, 373–376 (2010)

40. S.G. Kumar, K.K. Rao, Comparison of modification strategies towards enhanced charge carrier separation and photocatalytic degradation activity of metal oxide semiconductors (TiO_2, WO_3 and ZnO). Appl. Surf. Sci Part B. **391**, 124–148 (2017)

41. A. Houas, H. Lachheb, M. Ksibi, E. Elaloui, C. Guillard, J.-M. Herrmann, Photocatalytic degradation pathway of methylene blue in water. Appl. Catal. B Environ. **31**, 145–157 (2001)

42. P. Jongnavakit, P. Amornpitoksuk, S. Suwanboon, N. Ndiege, Preparation and photocatalytic activity of Cu-doped ZnO thin films prepared by the sol–gel method. Appl. Surf. Sci. **258**, 8192–8198 (2012)